Contact-free surface chemistry with acoustic levitation

SMARAGDA-MARIA ARGYRI

Department of Chemistry and Chemical Engineering
Chalmers University of Technology
Gothenburg, Sweden, 2022

Contact-free surface chemistry with acoustic levitation

SMARAGDA-MARIA ARGYRI

Department of Chemistry and Chemical Engineering
Chalmers University of Technology
SE-412 96 Gothenburg
Sweden
Phone: +46 (0)31 772 1000
www.chalmers.se

Cover: Illustration showing a multiple-transducers acoustic levitator with a self-standing droplet. The red and blue arrows illustrate the acoustic pressure and the surface tension, respectively.

Contact-free surface chemistry with acoustic levitation
SMARAGDA-MARIA ARGYRI
Department of Chemistry and Chemical Engineering
Chalmers University of Technology

Abstract

An ultrasonic acoustic levitator is a device that allows the implementation of contact-free studies by generating an airborne acoustic pressure field, capable of trapping, in mid-air, small volume samples ($< 10\,\mu$L) within the low-pressure areas (*i.e.*, nodes). Recent studies have improved the theoretical and experimental understanding of acoustic levitation, though, the performance of the device remains often far from ideal for the implementation of physicochemical studies.

In this licentiate thesis, three different designs of multiple-transducers acoustic levitators are presented and evaluated in terms of both simulated acoustic pressure and experimental performance. It was found that by tuning the cavity length of the device, it was possible to reduce the number of transducers while generating equally high acoustic pressure fields. Furthermore, the levitator with the densest packing of transducers exhibited the best performance, in terms of stability and levitation capacity. This framework can be applied in the customization of the design for specific applications.

A highly stable acoustic levitator was utilized for determining the surface tension of aqueous surfactant solutions through a data-driven approach. Approximately 50,000 photographs of acoustically levitated droplets were used for the training of a deep neural network while the predicting evaluation was based on $\sim$10,000 photographs. The mean absolute error of the neural network surface tension predictions was below 0.9 mN/m. The methodology presented here surpassed previous limitations related to droplet size and deformation, while generating equally high, and in specific cases higher accuracy.

Keywords: Acoustic levitation, surface chemistry, machine learning.

ii

List of Publications

I **Optimization of single-node single-axis acoustic levitator for contact-free mid-air experiments**
<u>Smaragda-Maria Argyri</u>, Nicolas Paillet, Lars Evenäs, Jens Ahrens, Carl Andersson, Victor Contreras, Asier Marzo, and Romain Bordes
Manuscript

II **Contact-free measurement of surface tension on single droplet using machine learning and acoustic levitations**
<u>Smaragda-Maria Argyri</u>, Lars Evenäs, and Romain Bordes
Submitted manuscript

My Contributions to the Publications

Paper I
Main author. Performed all experimental work and wrote the Python code, except code for simulations of acoustic pressure fields, frequency response plots, and Docker images for the online framework.

Paper II
Main author. Performed all experimental work, except the design and construction of the acoustic levitator. Built and evaluated the machine learning algorithm.

List of Abbreviations

SPL: Sound pressure level

ML: Machine learning

DNN: Deep neural network

NN: Neural network

MAE: Mean absolute error

MSE: Mean squared error

fps: Frame(s) per second

SDS: Sodium dodecylsulfate

CTAB: Cetyltrimethylammonium bromide

List of Figures

Contents

1

Introduction

The study of samples in a contactless manner opens up opportunities in the fields of chemistry and biology, where contamination and surface intervention need to be avoided. Numerous techniques have been developed for the levitation of samples, such as optical tweezers, magnetic levitation, electrostatic levitation, acoustic levitation, and others. All of these techniques allow the trapping of small volume samples (typically around 0.1-10 μL), crucial for biochemical studies [1], where the available volume may be limited (*e.g.*, blood samples from small animals [2]), or in cases, surface intervention needs to avoided (*e.g.*, omnidirectional drying). Acoustic levitation possesses an additional advantage, in that the sample does not need to exhibit magnetic or dielectric properties to be levitated. The main limitation is related to the weight of the sample, with respect to the acoustic forces applied to hold it aloft.

The most common acoustic levitator used in the past is called Langevin horn, in honor of Paul Langevin who together with Constantin Chilowsky developed an ultrasonic probe for submarine detection in 1917 [3, 4]. This device consists of a powerful transducer, that produces ultrasonic waves, and a reflector (Figure 1.1a). An airborne acoustic pressure field is generated when the transmitting and reflecting waves interact. Similarly to the case of a standing wave, the generated acoustic pressure field consists of areas of low (*i.e.*, nodes) and high pressure (*i.e.*, anti-nodes) that appear to be immovable in space. The nodes act as physical traps for objects with radius < 1.3 mm (for an operating frequency of 40 kHz), due to the

surrounding acoustic pressures, which drive the object towards a so-called home position. The upward force counteracts gravity, while if lateral forces exist close to the acoustic node, the movement of the levitated object will be more restricted (*i.e.*, spatial stability), than in the case where no lateral forces are present.
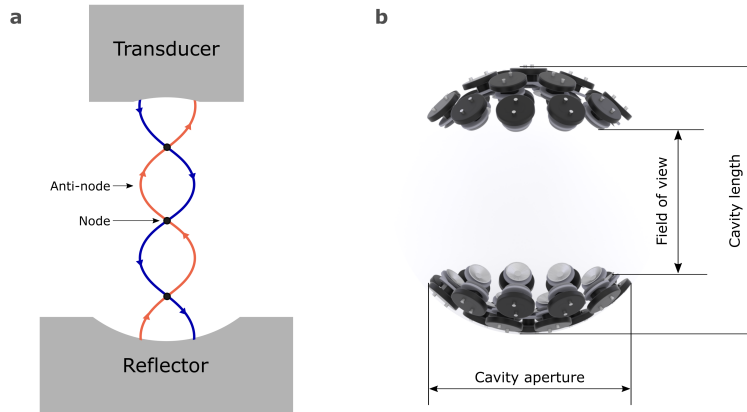
Figure 1.1: (a) Illustration of a Langevin horn and a simplified depiction of a standing wave being generated when the opposing acoustic waves (blue and orange line with arrows) interact. The acoustic nodes and anti-nodes denote the areas with the lowest and highest acoustic pressure, respectively. (b) Photorealistic illustration of a multiple-transducers acoustic levitator. The main designing parameters are illustrated.

The Langevin horn usually operates at a frequency of 25 kHz and it requires high voltage (> 100 V) since the acoustic field is generated by a single emitter [5, 6]. Although the device is simple to build, its performance can be highly sensitive to changes in humidity and temperature, thus requiring frequent tuning [6, 7]. Additionally, this type of levitator presents little to no lateral forces. As a result, positioning the sample inside the acoustic trap can be challenging, while the lateral spatial stability of the sample may be low during levitation.

The lack of spatial stability presented by Langevin horns has recently been tackled by new designs of acoustic levitators relying on multiple sources (Figure 1.1b). Arrays of multiple transducers have attracted a significant amount of attention, due to low cost, low driving voltage (< 20 V) and the possibility to subdivide the arrays into groups with different phases [8]. This allows rotational [9] and spatial control over

the levitated sample [10–13], while it provides the possibility to design customized acoustic levitators for different applications.

The designing (*i.e.*, number of transducers, arrangement, *etc.*), and operating parameters (*i.e.*, operational frequency, phase, *etc.*) of the acoustic levitator play a key role on the performance of the device, in terms of levitation strength and spatial stability of the sample. Recently, Marzo *et al.* [14] reported a new design of concave acoustic levitators, called TinyLev, which consists of multiple ultrasonic transducers and operates at a lower voltage (< 20 V). The design consists of 72 transducers in total, which are equally distributed into two concave planes of transducers, with a cavity aperture of 60 mm. The cavity length was 120.0 mm and the transducers were positioned in a circular arrangement. It was reported that the device could levitate samples with a density of up to 6.5 g/cm^3 and, without being highly influenced by environmental conditions. Furthermore, it has been shown that for the same number of transducers the maximum acoustic pressure increases, when the acoustic levitator was simulated to be more compact (*i.e.*, shorter cavity length and smaller radius of curvature) [14].

1.1 Purpose and objectives

Although currently used systems, such as TinyLev, offer many advantages, further improvements related to spatial stability, rotation, and levitation strength are required to reduce experimental noise and facilitate the use of acoustic levitation for physicochemical studies. Subsequently, two main objectives are defined and covered in Papers I and II. The first objective was to develop and evaluate the performance of new acoustic levitators, and the second was to illustrate the applicability of these devices in the implementation of surface chemistry studies. To illustrate the second objective, the study of surface tension was chosen owing to the fact that the acoustic pressure field can deform liquids to a different degree depending on the surface tension, volume, and applied acoustic pressure.

In Paper I, the influence of the main designing parameters of acoustic levitators (*i.e.*, number of transducers, cavity length, radius of curvature, and cavity aperture) were evaluated. Three different models of concave acoustic levitators (Mk1, Mk2, and Mk3) were developed and evaluated in terms of simulated acoustic pressure field

and experimental performance. Furthermore, an interactive online tool for the design of acoustic levitators was developed. This tool allows the user to define the desired design parameters and simulate in real-time the acoustic pressure field for the specific configuration. A suitable file for 3D printing can then be generated, which encourages the customization of acoustic levitators for practical applications.

In Paper II, the acoustic levitator Mk1 was utilized for the contact-free determination of surface tension of acoustically levitated aqueous surfactant solution droplets. A series of surfactant solutions were suspended and evaporated over a period of 30 min, while the voltage was varied simultaneously. A high-speed camera was utilized to collect images ($> 50,000$ images) of the levitated droplets. Following, pre-processing and data selection were performed and the selected data were fed into a deep neural network (DNN). The DNN was trained to uncover patterns in the data without any set preconditions that led to the determination of the surface tension of the droplets with a mean absolute error (MAE) of ± 0.88 mN/m.

Theory

This section is separated into three parts. The first part relates to the physics around acoustic levitation. The mathematical descriptions of the acoustic pressure field and acoustic radiation force applied on rigid and permeable objects are introduced. Then, the main electric properties of ultrasonic transducers are presented, as they are at the core of acoustic levitation. The second part focuses on the property of surface tension and previous attempts to determine it through acoustic levitation using a Langevin horn. In this work, the limitations of these attempts are addressed through machine learning. For that reason, the fundamentals of machine learning are introduced, in the third part.

2.1 Acoustic pressure field

Acoustic waves induce mechanical vibrations in a medium, which alter the pressure of the medium locally. In the case of simple sonotrodes, such as Langevin horns, a stable acoustic pressure field is generated through the interference of acoustic waves generated by the ultrasonic horn and opposing acoustic waves reflected by the reflector. In the case of multiple sources, the generated acoustic pressure field can be simulated through the summation of the individual pressures each source produces. The radiation pattern - also known as directivity - of the ultrasonic transducers refers to the pattern that the generated sound pressure level (SPL)

propagates in space. Depending on this pattern, different solutions to the wave equation are found.

Herein, we assume that each transducer acts like a point source and that the sound pressure propagates homogeneously around the point source like a circular ring. In that case, the acoustic pressure, p_j, is expressed as:

$$p_j = \frac{e^{ikr_j}}{r} J_0(kr_j \sin \theta_j) \qquad (2.1)$$

where, r is the effective radius of the transducer, r_j is the distance between the transducer j and the levitation point, k is the wavenumber, J_0 is the Bessel function of the first kind of order 0, and θ_j is the angle between the transducer and the z-axis.

2.1.1 Acoustic radiation force on rigid objects

When an object is introduced into the acoustic pressure field part of the acoustic waves will be scattered on its surface and the object will experience the so-called acoustic radiation force. This force can be described based on the scattering theory for rigid and permeable objects. Within the linear time-harmonic regime, the mass and momentum conservation equations in the medium are expressed as [15]:

$$\text{div}(\mathbf{v}) = i\omega p / K \qquad (2.2)$$

and,

$$-i\omega\rho\mathbf{v} = -\nabla(p) \qquad (2.3)$$

where, $\text{div}(\mathbf{v})$ is the divergence of the particle velocity, v, p is the acoustic pressure, K is the bulk modulus of the medium, which is defined as $K = \gamma P_0 \, \rho$, with γ being the adiabatic constant and P_0 the atmospheric pressure in ambient conditions, and ω

is the angular frequency. $\nabla(p)$ is the gradient of acoustic pressure, which is defined as:

$$-\nabla(p) = \left(\frac{\theta p}{\theta x}, \frac{\theta p}{\theta x}, \frac{\theta p}{\theta x} \right) \qquad (2.4)$$

By combining Equations (2.2) and (2.3), we acquire the Helmholtz equation [15]:

$$\Delta(p) = k^2 p = 0 \qquad (2.5)$$

where, k is the wavenumber and is defined as: $k = \omega/c$, where c is the speed of sound in the medium.

To solve the Helmholtz equation and thus acquire the pressure of the acoustic field around the object, we need to take the boundary conditions around the surface, Γ_j, of the object. We define the simplest case of a rigid (*i.e.*, non-permeable) object that is not moving in space. This means that the normal component, n_j, of the particle velocity will be zero. In that case, we can take the boundary conditions of the Neumann type:

$$\nabla(p) \cdot n_j = 0 \qquad (2.6)$$

To determine the normals, n_j we need to define the shape of the object. In case the object is spherical and small in comparison to the wavelength, the condition $ka \ll 1$ applies (where, k is the wavenumber and a is the radius of the spherical object). In this case, the acoustic radiation force is expressed as:

$$F = -\nabla U \qquad (2.7)$$

where, U is the Gor'kov potential:

$$U = 2\pi R^3 \left(\frac{\langle p^2 \rangle}{3\rho c^2} - \frac{\rho \langle u^2 \rangle}{2} \right) \tag{2.8}$$

In the case of an ellipsoidal object, the force applied to the object is different throughout the surface. To solve this case we need to derive the spheroidal Bessel functions that describe the surface. This case is relevant for liquids that can be deformed towards ellipsoidal shapes.

2.1.2 Acoustic radiation force on permeable objects

In the case of a permeable object, the acoustic waves will be partially absorbed by the object and partially scattered in all directions. The percentage of the acoustic wave intensity reflected on the boundary of the object depends on the difference between the acoustic impedance of the traveling medium (Z_1) and that of the object (Z_2). Where the acoustic impedance of a material is defined as:

$$Z = \rho v \tag{2.9}$$

And the intensity reflection coefficient, which describes the percentage of acoustic waves reflected is expressed as:

$$a = \left(\frac{Z_2 - Z_1}{Z_1 + Z_2} \right)^2 \tag{2.10}$$

where ρ and v are the density and the speed of the sound in the medium, respectively. For instance, in case the traveling medium is air ($Z_1 = 413 \ \mathrm{kg/(m^2 s)}$) and the levitated object is water ($Z_2 = 1.48 * 10^6 \ \mathrm{kg/(m^2 s)}$, at 20° C), then the intensity reflection coefficient, a is found to be 99.9%. Hence, only a small fraction of acoustic waves are absorbed by water due to the large density difference between the media.

For spherical objects the pressure field inside the object is expressed as [15]:

$$p_j^{in} = \sum X_n^j \zeta_n^j(r_j) \tag{2.11}$$

where,

$$\zeta_n^j(r_j) = J_n(k_j r_j)e^{in\theta_j} \tag{2.12}$$

where, X_m^j are complex coefficients, $\zeta_n^j(r_j)$ are the cylindrical wavefunctions and $J_n(k_j r_j)$ are the Bessel functions of the first kind.

Ultrasonic transducers allow the acoustic levitation of samples, due to nonlinear effects that result from the high-power acoustic waves involved. Hence, the analysis needs to be performed in the nonlinear regime. The medium is governed by the mass, momentum, and energy conservation equations:

Mass conservation:

$$\frac{D\rho}{Dt} + \rho \nabla \cdot v = 0 \tag{2.13}$$

where,

$$\frac{D\rho}{Dt} \equiv \frac{\theta}{\theta t} + v_i \frac{\theta}{\theta x_i} \tag{2.14}$$

Momentum conservation:

$$\rho \left(\frac{\theta v}{\theta t} + (v \cdot \nabla)v \right) = -\nabla p + \eta \Delta v + (\zeta + \frac{\eta}{3} \nabla^2 v) \tag{2.15}$$

Energy conservation:

$$\rho T \left[\frac{\theta s}{\theta t} + (v \cdot \nabla)s \right] = \kappa \Delta T + \zeta (\nabla \cdot v)^2 + \frac{1}{2}\eta (\theta_i v_j + \theta_j v_i) - \frac{2}{3}\nabla \cdot v \delta_{ij})^2 \quad (2.16)$$

where ρ is the density of the medium, v is the particle velocity, p is the pressure, t is time, x is the space coordinate, η is the dynamic viscosity, ζ is the bulk viscosity, $v = -\nabla \Phi$, with Φ being the velocity potential, κ is the heat conduction number, δ_{ij} is the Kronecker tensor. For the derivations and more information on nonlinear acoustics please refer to [16]. The theoretical framework presented above has been implemented in the Python library *Levitate* [17] and has been used as a tool for theoretical calculations in this project.

2.1.3 Piezoelectric transducers and electronic circuit

The main component of an acoustic levitator is the piezoelectric transducer. This device converts the electrical charge to mechanical vibrations and *vice versa*. As a result, a transducer can function both as an emitter and receiver of acoustic waves. When electric current is run through them, they vibrate and therefore generate acoustic waves in the ultrasonic regime. Conversely, if mechanical force is applied then a charge is produced. The relation between the applied charge, Q, and the force, F, generated is expressed as:

$$F = \frac{Q}{d} \quad (2.17)$$

where, d is the piezoelectric coefficient.

From Equation (2.17), it is evident that the higher the charge (*i.e.*, power) applied, the higher the amplitude of the force, and inversely the higher the force received, the higher the generated charge.

Furthermore, piezoelectric transducers can be described as a series resonance L-C circuit, where the electrodes on the piezo plate and the resonating mass act as a capacitor and an inductance, respectively [18]. Hence, the resonance frequency, f_{res} of the circuit is found when the capacitive reactance (x_C) and inductive reactance (x_L) are equal. Where:

$$x_C = \frac{1}{2\pi f C} \tag{2.18}$$

and,

$$x_L = 2\pi f L \tag{2.19}$$

Solving for Equations (2.18) and (2.19):

$$f_{res} = \frac{1}{2\pi\sqrt{LC}} \tag{2.20}$$

where, C is the capacitance and L is the electrical inductance of the circuit.

When the circuit operates at the resonance frequency, the impedance of the circuit is minimized, while the current consumption is maximized. Hence, the power transferred from the transducers to the medium reaches a maximum. In practice, transducers are not ideal components and the resonance frequency may be affected by the environmental conditions (*e.g.*, temperature, humidity *etc.*), the resonance of other transducers, and the voltage applied. For that reason, it is recommended to experimentally determine the resonance frequency of the circuit to ensure that it operates at the optimum frequency.

2.2 Surface tension and capillary length

Surface tension is a property of liquids that arises from the imbalanced cohesive forces among the molecules on the surface of the liquid. The molecules in the bulk experience cohesive forces in all directions due to the neighboring molecules. However, the molecules on the surface experience an inward net force, which aims to minimize the surface energy by minimizing the surface area of the liquid. The higher the cohesive forces between the molecules, the more energy is required to change the area of the liquid. Hence, in terms of energy, surface tension can be defined as the amount of energy required to increase the surface area by one unit area:

$$\gamma = \frac{W}{\Delta A} \tag{2.21}$$

where, W is the work and ΔA is the surface area difference.

The quantitative, empirical studies done by Thomas Young, in 1805 [19] and the mathematical analysis performed by Pierre-Simon Laplace, in 1807 [20], led to the so-called Young-Laplace equation, which correlates the pressure difference on the boundary between the medium (*e.g.*, air) and the liquid of study (Δp), to the surface tension (γ) and the total surface curvature of a liquid droplet ($\nabla \cdot n$), when in equilibrium:

$$\Delta p = -\gamma \nabla \cdot n \tag{2.22}$$

The pressure difference (ΔP) is also known as the Laplace pressure. For spherical droplets with radius, R, the Laplace pressure is defined as:

$$\Delta P = P_{\text{inside}} - P_{\text{outside}} = \frac{2\gamma}{R} \tag{2.23}$$

The shape of a free-standing droplet will therefore be governed by its surface tension and will tend to be spherical unless the hydrostatic pressure resulting from

the gravitational forces comes into play. Hence, the Laplace pressure increases as the size of the droplet decreases. The radius at which the Laplace pressure equilibrates the hydrostatic pressure is called capillary length (λ_c, Equation (2.24)) and defines a theoretical threshold above which the gravitational forces will have a greater influence on the shape of a droplet:

$$\lambda_c = \sqrt{\frac{\gamma}{\rho \, g}} \tag{2.24}$$

where, ρ is the density and g is the gravity acceleration.

2.2.1 Surfactants

Surfactants are molecules that consist of a hydrophilic part and a hydrophobic part, which prompts their surface activity. The surface activity of surfactants depends on numerous parameters (*e.g.*, length of hydrophobic part, charge, diameter of hydrophilic part, *etc.*), and depending on the charge of the hydrophilic part three main types of surfactants can be defined: anionic, non-ionic, and cationic. Surfactants tend to accumulate at interfaces between the polar phase (*e.g.*, water) and the non-polar phase (*e.g.*, oil or air), and when doing so, they reduce the surface tension. When the concentration of surfactants in solution reaches a critical concentration, the surfactants begin to self-assemble into spherical micelles, in order to reduce the free energy of the system. This concentration is called the critical micelle concentration (CMC), and above that value, the surface tension remains constant or reduces at a slower rate.

2.2.2 Determination of surface tension through acoustic levitation

An acoustically levitated liquid droplet will experience an acoustic radiation force, which will induce a degree of deformation from sphericity. As shown in Figure 2.1a-c, the degree of deformation depends on the volume, voltage (*i.e.*, acoustic pressure), and surface tension of the liquid. Specifically, in Figure 2.1a, the effect of droplet volume is shown for different droplets that have the same surface tension and experience the same voltage. It is observed that as the volume decreases, the

droplet will deviate less from sphericity because the droplet will experience a lower acoustic radiation force on its surface. In Figure 2.1b, it is shown that for constant volume and surface tension, the shape of the droplet will deviate from sphericity more as the voltage applied increases. The driving voltage defines the amplitude of the acoustic pressure generated by the transducers. As a result, the acoustic pressure will increase, as the driving voltage increases. Lastly, in Figure 2.1c, is shown the effect of surface tension when the volume and voltage are identical. It is observed that the deformation will be larger for lower surface tension, which is due to the lower capacity of the droplet to withstand the acoustic pressure applied.

The first attempt to produce a theoretical model that correlates the shape of an acoustically levitated droplet with the surface tension, γ, was performed by Trinh and Hsu [21]. The authors studied various substances with constant surface tension, with a Langevin horn. They calculated the acoustic radiation force according to the Gor'kov theory [22] and utilized the equations derived by Marston *et al.* [23] [24], to mathematically describe the equilibrium shapes of the acoustically levitated droplets, as:

$$r(\theta) = R + x(\theta) \tag{2.25}$$

where, R is the equivalent spherical radius of the droplet for a certain volume and $x(\theta)$ describes the deviation from sphericity as:

$$x(\theta) = -\frac{3}{64\gamma}(3\cos^2\theta - 1)R^2 P_s^2 \beta_0 \left(1 + \frac{7}{5}(kR)^2\right) \tag{2.26}$$

where, θ is the azimuth angle, β_0 and k are the compressibility and wavenumber of the host medium (*i.e.*, air), respectively.
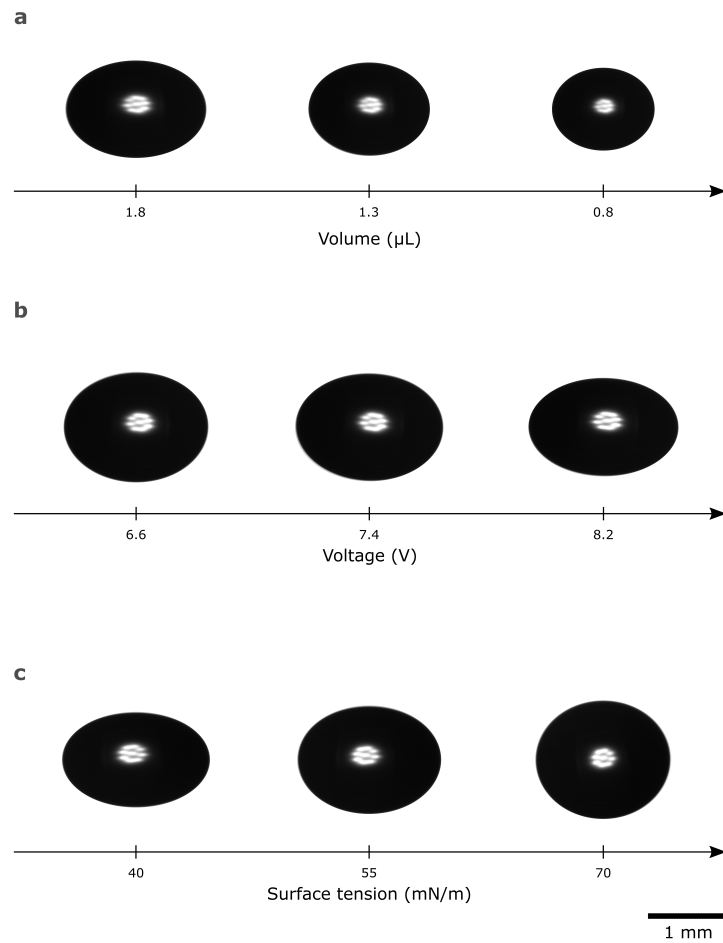
Figure 2.1: Relation between deformation of an acoustically levitated droplet with the (a) volume, for voltage of 9.0 V and surface tension of 29 mN/m (b) voltage, for volume of 2.1 µL and surface tension of 48 mN/m, and (c) surface tension, for volume of 2.0 µL and voltage of 7.0 V.

It should be noted that according to the Gor'kov theory [22], the Equation (2.26) is valid for spherical droplets with a maximum radius that is 1/10 of the operating wavelength of the device ($f = 25$ kHz, for Langevin horns). Another condition is that the radius must not exceed the capillary length of the liquid. Above the capillary length, the gravitational force will be higher than the Laplace pressure, hence, the levitated droplet will be flattened at the bottom, due to its own weight, which will induce an asymmetry. Lastly, the acoustic pressure applied on the

surface of the droplet needs to be calculated. This has traditionally been done with a microphone, however, non-linear acoustic effects present in the ultrasonic regime may significantly decrease the accuracy of the measurement of acoustic pressure [25].

A more detailed and analytical attempt has been reported by Tian *et al.* [5]. In this publication, an optimization algorithm to determine the shape and the position of an acoustically levitated droplet in space was developed. The shape of the droplet was described *via* a Legendre function. To determine the wave field inside the droplet, the authors derived a Bessel function after combining Green's function, Helmholtz formula, and the spherical Hankel function of first kind. The acoustic radiation pressure on the droplet surface was determined through an equation that correlated the sound pressure and particle velocity inside and outside of the droplet. Through a loss function and multiple iterations, they determined the Legendre constants and the Bessel coefficients by minimizing the difference between the derived sound intensity or aspect ratio in comparison to the experimental values measured with a microphone and the camera, respectively.

This algorithm was applied in a later publication by Tian *et al.* [26], to determine the surface tension of acoustically levitated samples. Overall, they reported a sensitivity of ± 2 mN/m for surface tension values lower than 50 mN/m. The authors stated that the reason the sensitivity was low in comparison to other techniques (typical statistical error: ± 0.5 mN/m) was related to low spatial stability of the acoustic levitator they were using.

It should be noted that in both studies mentioned above, a Langevin horn was used. Based on simulations (Supporting Information, Paper II), this acoustic levitator presents a simple acoustic pressure field, with no lateral forces. In contrast, multiple-transducers levitators generate a more complex pressure field, which applies omnidirectional acoustic radiation forces on the levitated sample. As a result, more complex equations than the ones presented here are required for the description of droplet deformation.

2.3 Machine learning

Machine learning is a statistical tool that can uncover patterns in large datasets without pre-assumptions, surpass heuristic model limitations, and accelerate the solution of computational and analytical challenges, like for example, in quantum computing [27]. Different types (*i.e.*, supervised, unsupervised, reinforced), and methods (*i.e.*, classification, regression), of machine learning algorithms, have been developed, in order to tackle different challenges.

In this section, we will focus on supervised deep neural networks (DNN) for regression analysis. On the whole, supervised machine learning aims to develop a regression function, f that correlates the input data, x with the predicted output parameter(s), $\hat{y}$, as:

$$\hat{y}(x) := f(x, W) \tag{2.27}$$

For this type of machine learning algorithm the desired output parameter(s) need to be known, for instance through experimental measurements. In machine learning terminology the values that are used for the training of the neural network (NN) are commonly called *True values*, while the ones the NN outputs after the training are called the *Predictions*. The machine learning algorithm develops and applies statistical approximations with no pre-set assumptions between the input and output, hence empirical and theoretical limitations employed in previous models may be surpassed. The neural network has access to a fraction of the data (*i.e.*, training dataset) which allows the adjustment of the model parameters also known as weights, W. The choice of these parameters is evaluated on the rest of the training dataset (*i.e.*, validation dataset) through a loss function and the final neural network is evaluated on the remaining data (*i.e.*, test dataset). The most commonly used loss function is the l^2 norm of the error between the output values, y and the predicted values $\hat{y}$ (*i.e.*, least-squares error function):

$$L(y, \hat{y}(X)) := ||y - \hat{y}(X)||_2^2 \tag{2.28}$$

The smallest component of a neural network is the neuron (Figure 2.2. Similarly to the biological neurons, these components receive certain inputs, they weigh them and calculate the weighted sum of these inputs. Then, this sum is passed through an activation function and if a certain threshold is exceeded the neuron is activated. Depending on the activation function the output of the neuron differs. It is common practice in the machine learning community to normalize the data, before passing them through the neural network. This is enforced to avoid unit dependencies and the weighing of features with higher values as more important [27]. To normalize the data, the minimum and maximum values of the training dataset of each feature are used. Then, the test dataset is normalized based on the values of the training dataset. This means that if the data are normalized in the range from 0 to 1, the test dataset may include values smaller than 0 and higher than 1.
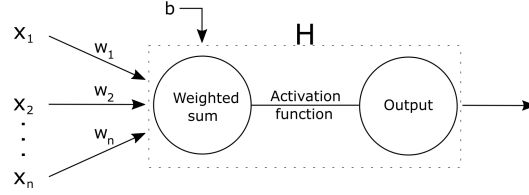

Figure 2.2: Illustration of a single artificial neuron, where X_n are the input data, w_n are the weights of each connection, b is the bias and H is the neuron (*i.e.*, perceptron).

In this work, two activation functions were utilized in the neural network, *softplus* (Equation (2.29)) and *swish* (Equation (2.30)):

$$f_{\text{softplus}}(x) = \frac{1}{\beta} ln(1 + e^{\beta x}) \tag{2.29}$$

and,

$$f_{\text{swish}}(x) = x \frac{1}{1 + e^{-\beta x}} \tag{2.30}$$

where, β is a scalable, trainable parameter.

18

In Figure 2.3, the activation functions are plotted, for $\beta = 1$. It is observed that the neuron will return zero in the case the input is smaller than -3 and -5 for *softplus* and *swish*, respectively. Although the data are normalized from 0 to 1, the probability of the neuron being activated or not depends on the values of the weights and bias (Figure 2.2).
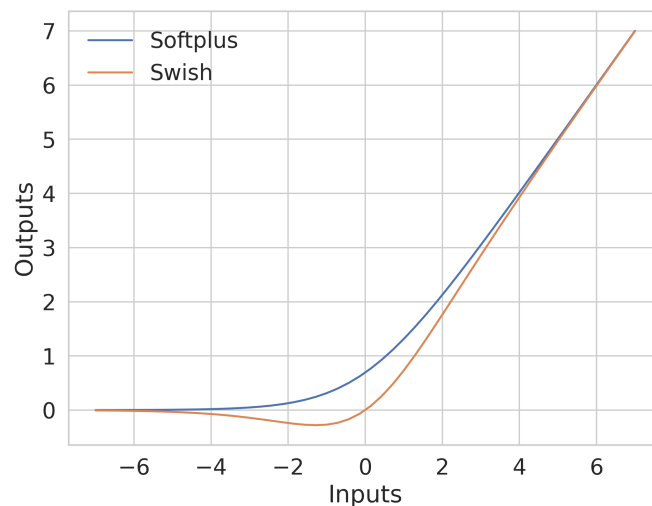

Figure 2.3: Activation functions that were used in the deep neural network in this work. Blue line: *softplus* function, orange line: *swish* function. In both cases β was set equal to 1.

In case the neural network is composed of less than 5 layers, it is referred to as a shallow neural network. Otherwise, it is referred to as a deep neural network. Depending on the application different neural network architectures are required. In Figure 2.4, the schematic form of a neural network is illustrated. The input parameters, X_n are passed through the layers, H_n, and the final output, O is calculated. This output is called the *target feature* and refers to the predicted value of the neural network for a certain case.
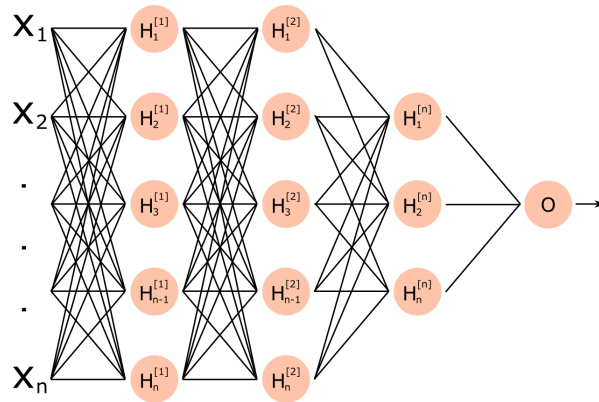
Figure 2.4: Schematic illustration of a neural network. The input data of a certain case, the neuron, and the predicted output (*i.e.*, target feature) are noted as X_n, H_n and O, respectively.

<div style="text-align: right">

3

</div>

Materials and methods

3.1 Chemicals

The following chemicals were used. Sodium dodecylsulfate (SDS) was obtained from Merck, cetyltrimethylammonium bromide (CTAB), and octylphenol decaethylene glycol ether (TritonX-100) were purchased from Sigma-Aldrich Sweden AB.

3.2 Construction of acoustic levitators

The open-source software OpenScad was used for the design of the scaffolds of acoustic levitators, which were 3D printed with polylactic acid (PLA). An oscilloscope and a customized setup were used for the identification of the phase of the ultrasonic transducers (Manorshi, MSO-P1040H07T). The operating frequency of the transducer was set at 40 kHz through an Arduino Uno board, while an L298N H-bridge was used for amplifying the driving signal.

3.3 Simulations of acoustic levitators

The simulations of the acoustic pressure field for different transducer configurations were performed with the Python library *Levitate*, developed by Carl Andersson, at

Chalmers [17]. Initially, the position of the transducers was introduced in Cartesian coordinates. Following, the directivity pattern of the transducers (*i.e.*, pattern of acoustic wave propagation from a sound source) was described as a circular ring with an effective radius of 3 mm, while the parameter p_0 that defines the pressure an ultrasonic transducer induces at 1 m, was set to 1 Pa.

The construction of the acoustic pressure field was performed by summing up the individual acoustic pressures each transducer generates. The acoustic pressure of a single transducer was described through Equation (2.1).

The simulations were performed for two different cases depending on the phase difference between the upper and bottom planes of transducers. When the transducer planes were in phase, the phase difference was 0, while when the phase difference was π, then the planes were in phase opposition.

3.4 Evaluation of experimental performance

3.4.1 Circuit frequency response

The circuit frequency response of the levitators was investigated at a constant voltage by varying the driving frequency and measuring the current consumption. The resonance frequency is found at the frequency where the current consumption reaches a maximum. At that frequency the performance of the device is optimum. Two different cases were studied based on whether the two upper and bottom halves were facing each other or not. The transducers have the ability to act both as an emitter and a receiver, for that reason it is important to record their behavior in terms of frequency for different transducer configurations and phases. In the case where the two halves do not face each other, then only the emitting circuit frequency response of the transducers will be recorded. The frequency response was studied when the transducer planes were in phase, and in phase opposition. The measurements were repeated three times.

3.4.2 Spatial stability

The spatial stability of the levitators was investigated at three different voltages (7 or 7.5, 10, and 12 V) by recording photographs of Milli-Q water droplets with a digital camera (acA1440-220um, Basler, Germany, operated at 1 frame per second (fps)) over a period of 10 min. From the recorded photographs, the volume, and center (x_c, z_c) of the droplets were extracted. The volume of the droplets was in the range of 0.5 to 5 µL. The measurements were repeated three times and the moving standard deviation, over a sliding window of length equal to 10 frames was calculated to observe potential dependencies between the volume and the stability. The average standard deviation from the three sets of measurements was plotted with respect to the applied voltage.

3.4.3 Levitation capacity

The strength of the acoustic field of each levitator was experimentally evaluated in the normal (*i.e.*, vertical) and perpendicular (*i.e.*, horizontal) orientation by determining the minimum voltage, V_{min} required to levitate a solid, spherical silica bead with mass, $m = 7$ mg and radius, $r = 1.8$ mm. For the normal orientation (Figure 3.1a), the silica bead was levitated at 8 V and then the voltage was gradually decreased until the silica bead was no longer able to be suspended. Regarding the perpendicular orientation (Figure 3.1b), the starting voltage was set at 25 V and was gradually reduced. The measurements were repeated three times and the standard deviation was calculated.
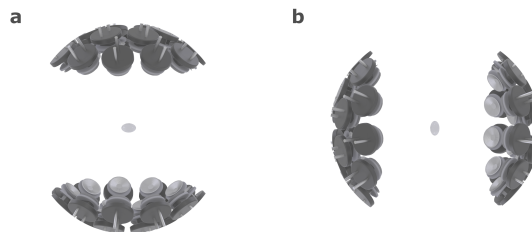

Figure 3.1: (a) Normal (*i.e.*, vertical) operating orientation of an acoustic levitator, and (b) perpendicular operating orientation to the normal one (*i.e.*, horizontal) of an acoustic levitator.

The levitation force per voltage was calculated based on the weight of the silica bead over the applied voltage as:

$$C_{\text{lev}} = \frac{m * g}{V_{\text{min}}} \qquad (3.1)$$

where, m is the mass of the silica bead, and g is the acceleration constant ($9.81\,\text{m/s}^2$).

3.5 Pendant drop method

The surface tension of the surfactant solutions was measured with the pendant drop method, with an Attension Theta optical tensiometer, by Biolin Scientific, Finland. The measurements were conducted at room temperature. A minimum of 10 droplets were formed by using a 0.718 mm (22 gauge) stainless steel needle. A black and white digital camera was used to record images of droplets and the surface tension was determined by fitting the Young-Laplace equation on the contour of the droplet. The surface tension of one solution was determined by averaging the values from the 10 droplets.

3.6 In-silico data for machine learning

In-silico contours were generated by using the volume (0.5 - 2.5 µL), acoustic pressure (1.5 - 4 kPa), and surface tension (30 - 72 mN/m), as inputs in Equation (2.25). Then, the physical conditions related to the size and shape of the droplets, that restrict Equation (2.25) were applied, to ensure that the contours had physical validity.

To simulate the way the contour coordinates are extracted experimentally, 900 random coordinates around the contour were extracted from Equation (2.25). From these coordinate points, 175 were chosen for constant polar coordinate, ϕ. To ensure that the angle ϕ was kept constant for all contours, linear interpolation through the 900 initial coordinates was applied. This step was important for the machine

learning training in order to remove the polar angle, ϕ (since it is kept constant for all contours) from the NN input features. Hence, the number of features was reduced while consistency between the features related to the contour was ensured. The 175 polar radii, r, and the acoustic pressure were the chosen input features for the training, while the surface tension was set as the target feature.

Artificial noise was added to the in-silico contours, to evaluate the effect that simulated experimental error may have on the model. Two main sources of experimental error were considered: having a non-well-defined contour due to blurriness, or a tilted contour. Blurriness may occur due to instabilities, while tilting is the result of not having the camera and the levitator properly aligned. The pixel accuracy of the camera is in the range of ± 0.5 pixels and the experimentally observed blurriness lies in the range of ± 3 pixels. Hence, the blurriness in the simulated contours was induced by adding a random value in the range of ± 0.5 to ± 5 pixels, with an interval of 0.5 pixels. Based on the calibration factor of the experimental set-up, 0.5 pixels correspond to approximately 2 μm. So, the contours were disturbed by approximately ± 2 μm to ± 20 μm. Experimentally, the maximum tilting angle observed was approximately 5°. However, since the majority of the in-silico contours are circular, little to no difference was observed for tilting angles between 0° to 5°. Hence, to investigate the effect of the tilting on the model, the range of tilting angles was set between 0° and 25°. In both cases, the training of the machine learning algorithm was repeated 6 times, and the MAE was used as the evaluation parameter.

3.7 Acquisition of experimental data

Series of aqueous solutions of SDS, CTAB, and TritonX-100 (10^{-7} - 10^{-1} M) were prepared in milli-Q water, at 23° C. The aqueous surfactant solutions were stored at room temperature. The acoustic levitation measurements were acquired within a maximum of three days after the solution was prepared. A plastic syringe with a steel needle was utilized to introduce a droplet into the acoustic field. Three droplets were levitated from each surfactant solution. Each droplet was individually evaporated while being acoustically levitated at the central acoustic node over a period of 30min. The digital camera (acA1440-220um, Basler, Germany) was set to capture images with a frame rate of 1 frame per second (fps), while the voltage varied with a rate

of approximately 0.05 V/sec. A Python code was developed to detect the contour of the droplet, determine the coordinates and calculate various droplet characteristics, such as radius, volume, aspect ratio, position, *etc.*. Furthermore, the voltage, current, and time at which each image was taken were recorded. The extracted contours were corrected for tilting (maximum tilting angle experimentally observed: 5° - 6°) and for the relative vertical position.

3.8 Data pre-processing for machine learning

The polar radius, *r* was determined *via* interpolation between the over 900 points the contour extraction function could identify and were equally distributed around the contour, by choosing the radius of the contour for a constant angle ϕ. The voltage and current were used as features, in replacement to the acoustic pressure, while the average vertical position was also used as a feature relevant to the acoustic pressure, as the position of the droplet varies with it. The average vertical position was calculated with respect to each individual droplet to set a common baseline. Furthermore, the contours were corrected with respect to potential tilting. In the case of tilted contours, the polar angle, ϕ, will not be the same consistently. Hence, the polar radius, *r*, will not correspond to the correct value. Furthermore, since the experimental contours are more compressed than the in-silico ones, a tilted contour may significantly influence the polar radius, *r*, as a feature.

3.9 Machine learning algorithm

Initially, the machine learning approach was evaluated on approximately 50,000 contours generated through the in-silico model. The chosen features were 175 polar coordinates, *r*, describing each contour and the acoustic pressure, while the surface tension was the target feature. DNNs can be susceptible to features that have higher numerical values, which can induce bias in the neural network and may lead to false predictions. For that reason, all features were normalized column-wise from 0 to 1. Initially, the dataset was split into training (80% of the total dataset) and test (20% of the total dataset) subsets. The 0 to 1 normalization was applied to the training subset and the test subset was normalized based on the range of the training features. The polar radius, *r*, was normalized with respect to the minimum and

Layer (type)	Output Shape	No. Parameters
Layer 1 (Dense)	(None, 50)	8,950
Layer 2 (Dense)	(None, 40)	2,040
Layer 3 (Dense)	(None, 30)	1,230
Layer 4 (Dense)	(None, 20)	620
Layer 5 (Dense)	(None, 15)	315
Layer 6 (Dense)	(None, 10)	160
Layer 7 (Dense)	(None, 5)	55
Layer 8 (Dense)	(None, 1)	6

Table 3.1: Architecture of the developed neural network for the prediction of surface tension of self-standing droplets. The output shape defines the number of neurons present in each layer and the number of parameters are shown in the last column. The total number of trainable parameters was 13,376.

maximum values among the droplets in the training subset so that the size ratios can be retained.

The architecture of the DNN that was developed is shown in Table 3.1. The model consists of 8 layers, with 50, 40, 30, 20, 15, 10, 5, and 1 neuron(s). The activation function swish was used in layers with an odd number (1, 3, 5, and 7) while the activation function softplus was applied in layers with an even number (2, 4, 6, and 8). The loss function was monitored by the Mean Squared Error (MSE) and the optimization function Adam was used. During training, only the training subset is used. This subset is split into 2 subsets, which consist of 80% of the data used for learning and 20% used for validation.

The MSE and the MAE of the learning and validation subsets are plotted with respect to the number of iterations (epochs) performed during the training. That way we can evaluate whether the model performs equally well during the learning and the validation, or if there are inconsistencies. If the learning and validation curves do not overlap, it means that the model may either overtrain (*i.e.*, performs better on the learning dataset, in comparison to the validation one) or undertrain (*i.e.*, performs better on the validation dataset, in comparison to the training one). The predictions of surface tension the model generated were compared to the values that were used as inputs in Equation (2.25) (*i.e., True values*, in machine learning terminology).

Additionally, the error distribution was plotted to better evaluate the error range of the model.

The performance of the machine learning algorithm was examined on the same in-silico data but with added noise and then on experimental data. More than 50,000 contours from the experimental data were used for the training. These contours belonged to a series of surfactant solutions that covered well the adsorption isotherm of each surfactant. The features that were used in this case were: 175 polar radii, r, for constant polar angle, ϕ, the voltage, the current, and the position of the center of the contour on the z-axis. The voltage and current were used as features, in replacement of the acoustic pressure. The vertical position was also used as a feature relevant to describe the acoustic pressure. The features were normalized in the same manner as for the in-silico contours and the same model architecture and evaluation were applied.

3.10 Determination of the importance of the features

A permutation feature importance algorithm, introduced by Fisher, Rudin, and Dominici [28] was applied to investigate the effect of each feature on the predictions. Initially, the MAE of the neural network without permuting the features was determined by predicting on the test dataset, after training. Following, the first feature was permuted by shuffling the specific column and predicting on the new test dataset. The resulting MAE was recorded. The same procedure is repeated until all features have individually been permuted and the resulting MAE is saved. The feature importance is calculated by subtracting the MAE of the original test dataset from the resulting MAE of the permuted feature. The procedure was repeated three times. The importance of a specific feature depends on the MAE increase after permutation. In case a high resulting MAE is recorded it means that the permuted feature had a high influence on the neural network predictions. It should be noted that this analysis is utilized as an evaluation tool for the choice of features used for the training, and whether this choice has a physical meaning, not to add interpretability to the neural network.

4

Results and discussion

4.1 Design of acoustic levitators

The design of the acoustic levitator reported by Marzo *et al.* [14] in 2017, referred to as TinyLev, was a major improvement compared to a simple sonotrode. However, its performance was often too limited for its use in physicochemical studies where ease to operate and stability are of prime importance. Therefore, three customized acoustic levitators, namely Mk1, Mk2, and Mk3, were theoretically and experimentally examined in terms of acoustic pressure, circuit frequency response, spatial stability, and levitation capacity.

The designs were inspired by the acoustic levitator TinyLev. Specifically, the first two designs (*i.e.*, Mk1 and Mk2) were more compact versions of TinyLev. In both cases, the transducers were placed on a concave plane with a circular configuration and were operating at 40 kHz. According to Adamowski *et al.* [29], positioning the transducers on a concave plane improves the performance of the acoustic levitator by concentrating the acoustic force locally.

The acoustic levitator Mk1 (Figure 4.1a and Figure 4.1a) consisted of fewer ultrasonic transducers in comparison to TinyLev (34 instead of 72) and the distance between the upper and lower plane of transducers was shorter (52.1 mm instead of 120.0 mm). The changes aimed at creating a more compact and stable acoustic levitator by further focusing the acoustic radiation forces. The size of the second

design, Mk2 (Figure 4.1b and Figure 4.1b) was further decreased in comparison to Mk1, with the hypothesis that the local acoustic pressure around the central node will increase, leading to higher spatial stability and overall better performance of the levitator. Levitator Mk2 consisted of 24 transducers and the distance between the two transducer planes was 38.1 mm.

As shown in Figure 4.2a-b, the arrangement of the transducers in the cases of Mk1 and Mk2 is circular. In contrast, levitator Mk3 (Figure 4.1c) was designed so that the transducers are arranged in a hexagonal arrangement. This allowed the maximum packing of the transducers, which aimed at further increase of the performance by increasing the local acoustic pressure around the node. Levitator Mk3 consisted of 36 transducers and the cavity length was 41.6 mm. The two planes are parallel but rotated by 60° with respect to each other so that the transducers are positioned symmetrically around the central node.

4.1.1 Simulation of acoustic pressure field

Various acoustic pressure fields will be generated depending on the arrangement, orientation, phase, and distance between the transducers. The Python library *Levitate* was utilized to simulate the acoustic pressure field for each designed levitator. In Figure 4.1d-i, and Figure 4.2d-f, the simulations of the acoustic pressure field each acoustic levitator generates, in the xz, yz, and xy directions are shown.

It can be observed that acoustic levitators Mk1 and Mk2 present equally high maximal acoustic pressure on the xz and yz planes (∼1200 Pa). This shows that by adjusting the cavity length, it is possible to achieve the same acoustic pressure level with fewer ultrasonic transducers. Additionally, it is evident that the acoustic pressure fields of Mk1 and Mk2 in the xz and yz planes are identical due to the symmetrical positioning of the transducers among the two transducer planes. In contrast, the acoustic pressure field of acoustic levitator Mk3 along the xz and yz planes (Figure 4.1d-i) exhibited different patterns, due to the hexagonal arrangement of transducers and the 60° shift between the transducer planes. More importantly, Mk3 presented the highest acoustic pressure in comparison to the previous designs. This is attributed to the hexagonal arrangement of the ultrasonic transducers, which allows the maximum possible packing of the transducers. As a

result, the acoustic beam is optimally focused, which improves the acoustic strength of the pressure field.
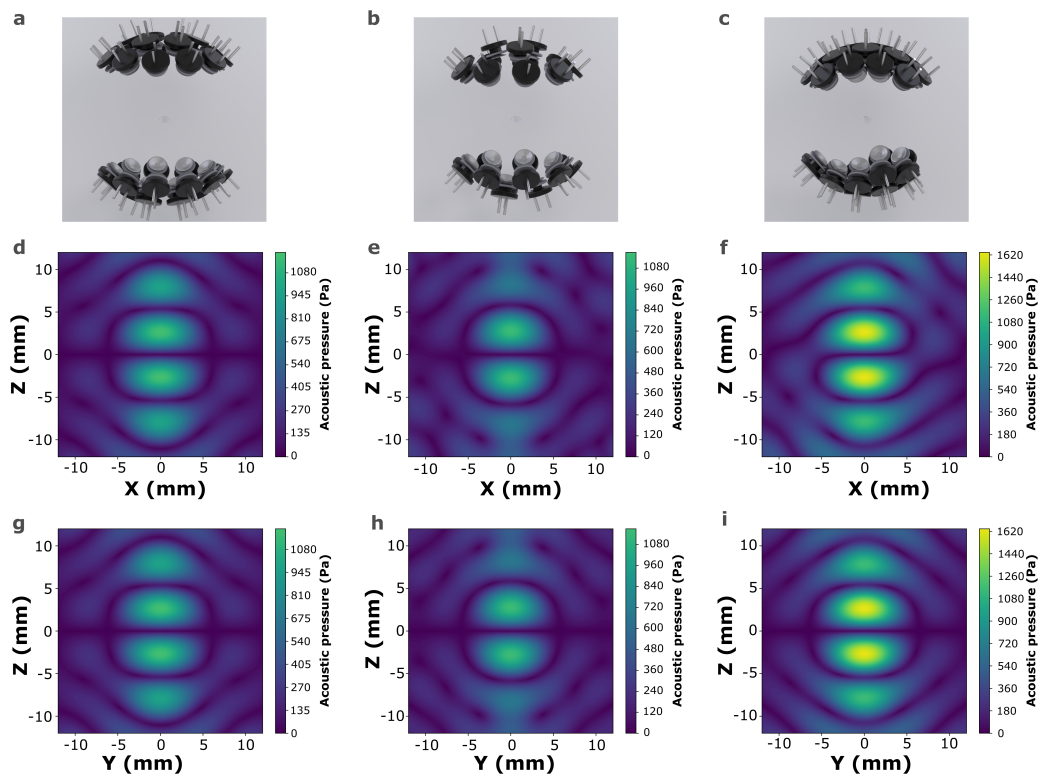

Figure 4.1: (a-c), Photorealistic rendering of acoustic levitators Mk1, Mk2, and Mk3, respectively, as viewed from the front (d-f) 2D simulations of acoustic pressure fields along the xz plane, and (g-i) along the yz plane.

Levitator Mk3 presented the highest acoustic pressure along the xy plane, followed by Mk2, while Mk1 exhibited the lowest acoustic pressure (Figure 4.2d-f). Furthermore, it is observed that the central area where the acoustic pressure is close to zero can be approximated by a circle with a radius of approximately 2.5 mm for Mk3 and approximately 8 mm for Mk2. Hence, the Mk3 design generates stronger lateral forces closer to the acoustic node, which is expected to restrict the movement of the levitated sample more in comparison to Mk2 and Mk1.
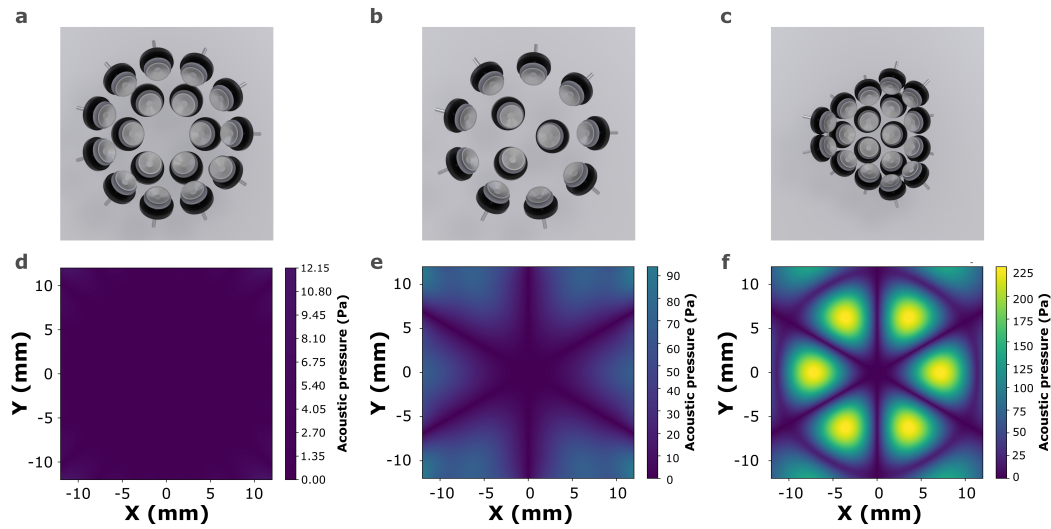
Figure 4.2: (a-c), Photorealistic rendering of acoustic levitators Mk1, Mk2 and Mk3, respectively, as viewed from the top, (d-f) 2D simulations of acoustic pressure fields along the xy plane.

4.1.2 Circuit frequency response

As mentioned in Chapter 2, the resonance frequency of ultrasonic transducers changes depending on the voltage applied through the circuit. An acoustic levitator performs best when it operates at its resonance frequency and worsens farther away from the resonance peak. Hence, it is important to evaluate to what degree the resonance frequency is affected by the voltage applied. Furthermore, ultrasonic transducers act both as emitters, and receivers of acoustic waves. For that reason, we defined two different cases where the two transducer planes are either opposing or not so each other. The measurements were repeated for two subcases where the transducer planes were either in phase or in phase opposition.

Figure 4.3a-c, shows the frequency responses of levitators Mk1 (black lines), Mk2 (blue lines), and Mk3 (green lines) at three different voltages (7, 10, and 12 V), while the two transducer planes are in phase, and opposing each other. The plots are normalized with respect to the number of transducers of the levitator. It is observed that two prominent frequency peaks are present at all three different voltages, for all three designs. The first peak is between $38 - 39\,\text{kHz}$ and the second one is between

$40 - 41$ kHz. As the applied voltage increases, the lower frequency peak shifts to the left, while the peak closer to 40 kHz shifts to the right for all acoustic levitators.

Figure 4.3d-f shows the circuit frequency response of the acoustic levitators when the two transducer planes were in phase opposition, and still facing each other. We can identify one main peak in most cases, however, for levitator Mk2 a second peak at lower frequencies tends to broaden the main peak as the applied voltage increases. A similar tendency is observed for the acoustic levitator Mk3, however, the discrepancy from the main peak is here clearer. Furthermore, a smaller peak is observed for Mk3 at a higher frequency.
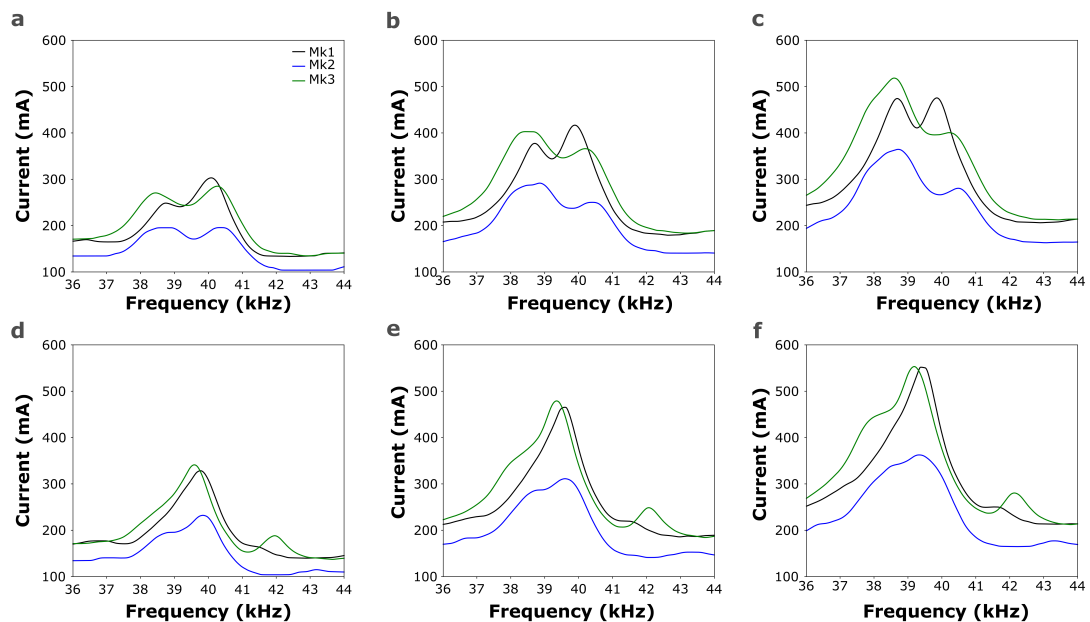
Figure 4.3: Circuit frequency response of levitators Mk1 (black), Mk2 (blue) and Mk3 (green) at 7, 10, and 12 V, (a-c) in the case where the two planes are in phase, and (d-f) in phase opposition.

To examine whether the different patterns observed, when the two transducer planes are either in phase or phase opposition, were related to the acoustic wave interference among the waves, the circuit frequency response of Mk1 was recorded when the two transducer planes did not oppose each other. Regardless of the

operating phase difference between the transducer planes, the same circuit frequency response pattern is recorded (Figure 4.4). Hence, it is evident that the different circuit frequency response patterns, exhibited in Figure 4.3, are the result of the acoustic wave interactions between the two transducer planes. Another important observation is that the resonance peak shifts from 39.9 kHz at 7 V, to 39.6 kHz at 10 V, to 39.5 kHz at 12 V. This is attributed to the increase in capacitance of the transducer as the voltage increases, in accordance with Equation (2.20).
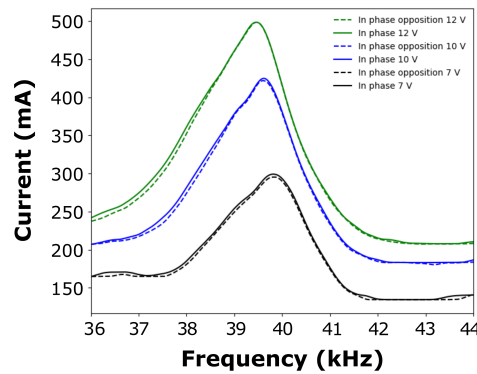
Figure 4.4: Circuit frequency response of acoustic levitator Mk1 when the ultrasonic transducer planes do not interact.

4.1.3 Levitation capacity

Table 4.1 presents the minimum voltage required by each acoustic levitator to suspend a silica bead with the weight of 7 mg, when the levitator was positioned vertically (normal orientation) and horizontally (perpendicular orientation), as illustrated in Figure 3.1.

It can be observed that levitator Mk1 presented the lowest levitation capacity since higher voltage was required to sustain the silica bead in the normal and perpendicular orientation, in comparison to Mk2 and Mk3. Levitator Mk2 could sustain the silica bead at a slightly lower voltage in comparison to Mk1, however, the values were close. In contrast, levitator Mk3 can sustain the silica bead in the air at 6.5 and 14.4 V when the device was operating in normal and perpendicular orientation, respectively (see Figure 4.5).

Orientation/Levitator	Mk1 (V)	Mk2 (V)	Mk3 (V)
Normal orientation	9.3 ±0.2	8.9 ±0.2	6.5 ±0.2
Perpendicular orientation	20.8 ±0.2	20.5 ±0.2	14.4 ±0.2

Table 4.1: Minimum voltage required by each acoustic levitator to suspend a 7 mg silica bead before dropping.

From Figure 4.5 the levitation force per voltage (Equation (3.1)) for each acoustic levitator presented. It is evident that levitators Mk1 and Mk2 exhibit similar levitation strength per voltage, while Mk3 had higher performance. The levitation capacity results were in agreement with the simulations of the acoustic pressure fields since levitators Mk1 and Mk2 presented equally high maximum acoustic pressure close to the central node on the xz (Figure 4.1)d-e and the yz (Figure 4.1)g-h planes, while Levitator Mk3 presented the highest maximum acoustic pressure close to the node in all dimensional planes, compared to the previous models.
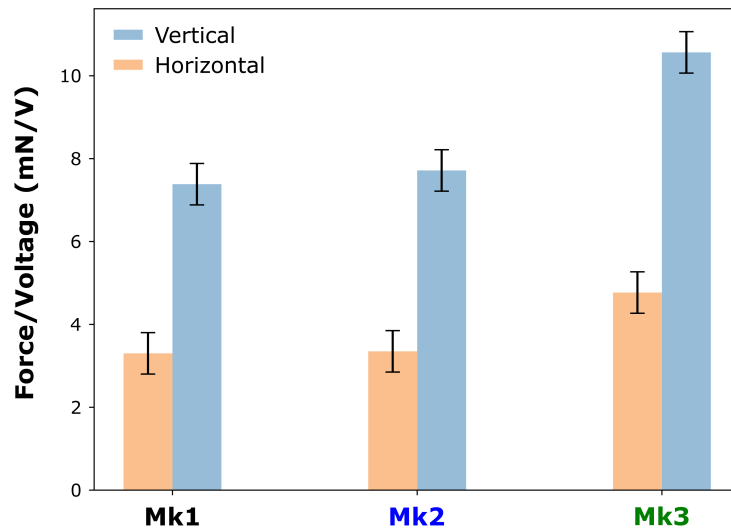

Figure 4.5: Comparison of the levitation force per voltage each acoustic levitator exhibited at vertical operating orientation (blue columns) and horizontal operating orientation (orange columns) for levitators Mk1, Mk2, and Mk3.

4.1.4 Spatial stability

The spatial movement of the levitated object was evaluated on water droplets over a period of 10 min, at three different voltages (7 or 7.5, 10, and 12 V). The advantage of evaluating the stability of an acoustic levitator with a liquid is twofold: (*i*) it relates to the intended use of the levitator for physicochemical studies of soft matter, and (*ii*) it can show whether there is a dependency between the stability and the volume of the sample. In Figure 4.6, the average standard deviation of the center (x_c, z_c) of the levitated water droplets is plotted with respect to the applied voltage along the horizontal, x-axis (upper plot) and vertical, z-axis (bottom plot) movement. In terms of stability along the horizontal, x-axis, it is observed that the samples levitated with Mk3 presented the least movement, followed by Mk1 and then Mk2. Along the vertical, z-axis, levitator Mk3 presented anew the highest stability, but in this case levitator Mk2 presented higher stability than Mk1 at 12 V, and similar stability, within the experimental uncertainty for voltage equal to 10 V or lower.
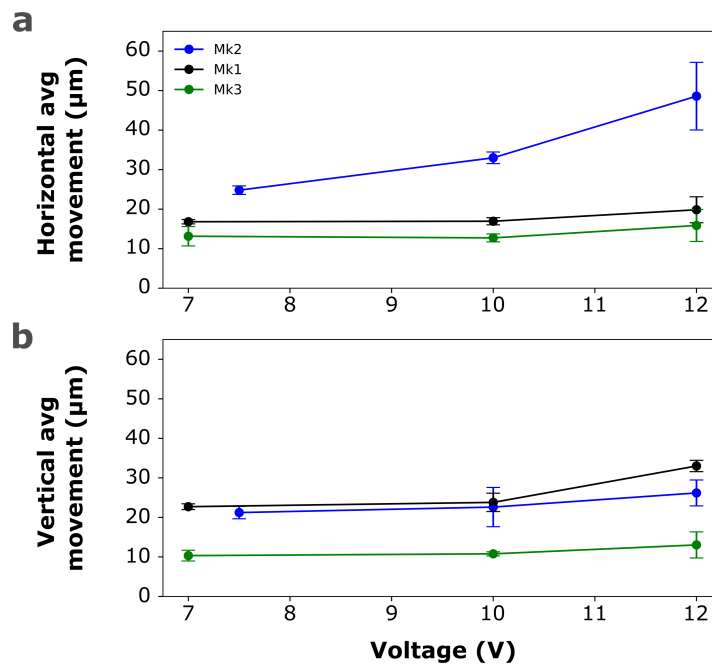

Figure 4.6: The average standard deviation of the center (x_c, z_c) of levitated water droplets is plotted with respect to the applied voltage for acoustic levitators: Mk1 (black), Mk2 (blue) and Mk3 (green), along (a) the x-axis and (b) the z-axis.

The high spatial stability presented by levitator Mk3, in comparison to the other two designs, was supported by the simulations of the acoustic pressure fields (Figure 4.1d-f and 4.2g-i). The fact that levitators Mk1 and Mk2 presented similar stability along the z-axis was also in accordance with the acoustic pressure levels along the xz and yz planes. However, levitator Mk1 presented higher stability along the horizontal, x-axis in comparison to Mk2, even though the latter presented higher lateral forces, based on the simulations of the acoustic pressure fields (Figure 4.2d-f). This may be attributed to the fact that the lateral forces produced by Mk2 are significant for distances larger than 5 mm around the center of the node (Figure 4.2e). Since the diameter of the levitated sample usually does not exceed 2 mm, it may be that the existing lateral forces do not confine the droplet movement sufficiently. Another possibility is that the generated force field of levitator Mk2 may present rotational components, due to higher curl forces, which according to Andersson *et al.* [30] can lead to higher instability. However, further investigation is required to verify this hypothesis.

4.2 Application of acoustic levitation to the determination of surface tension with machine learning

As explained in Chapter 2, an acoustically levitated microliter liquid droplet will be deformed due to the acoustic pressure field. The degree of deviation from sphericity depends on the volume, acoustic pressure, and surface tension (Figure 2.1). The resulting droplet deformation can be described from the balance of forces on the surface of the droplet. Hence, acoustic levitation can be an excellent tool for the determination of surface tension in a contact-free manner. However, the main difficulty arises from the accurate theoretical and experimental determination of the applied acoustic radiation force. Additionally, theoretical models apply simplifications and conditions that can limit the accuracy and applicability of the model. Machine learning does not rely on preconditions, thus allowing the uncovering of new correlations between the data. The customized levitator Mk1 provided sufficient stability for the acquisition of a large experimental dataset, required for the training of a neural network. To validate this data-driven approach, in-silico data were generated from Equations (2.25) and (2.26) with and without artificial noise. Then, the same neural network architecture was implemented on experimental data. The input features on which the neural network relied the most,

and potential droplet size and deformation limitations on the prediction of surface tension, were investigated.

4.2.1 In-silico data

The data distributions of the input parameters (*i.e.*, surface tension, volume, acoustic pressure) of Equation (2.25) after applying the physical restrictions related to the deformation and the size of the droplet (Chapter 3) , are shown in Figure 4.7a-c. Examples of representative contours generated based on those parameters are shown in Figure 4.7d.
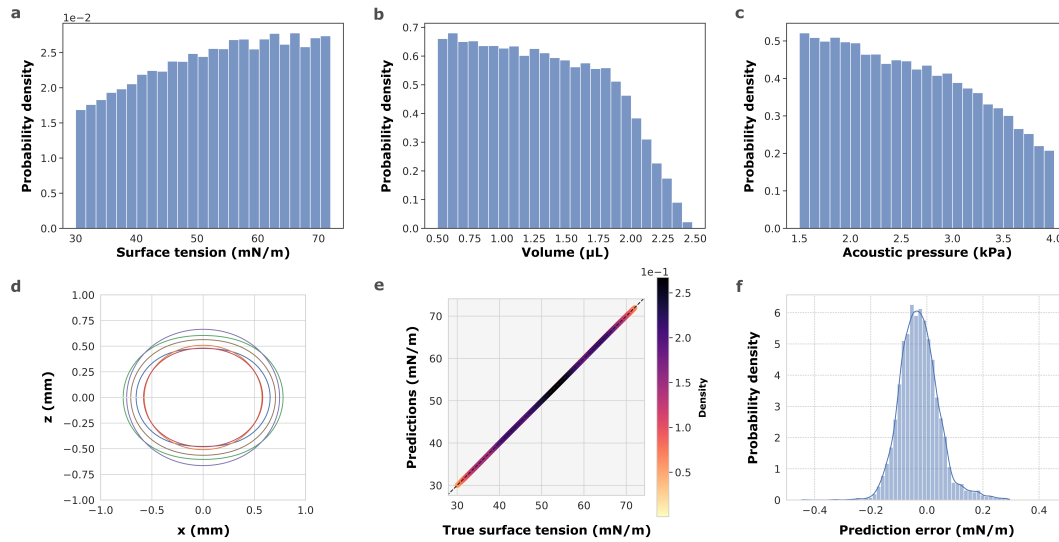

Figure 4.7: Data distributions of the input parameters after the conditions of Equation (2.25) were applied: (a) surface tension, (b) volume, (c) acoustic pressure. (d) Representative overlapping contours generated through Equation (2.25). (e) Comparison between the surface tension values from Equation (2.25) (x-axis) and the surface tension values predicted through the ML algorithm (y-axis). (f) Error distribution of the surface tension predictions the ML algorithm generated.

The performance of the ML algorithm in predicting the surface tension from in-silico contours is displayed in Figures 4.7e-f. In Figure 4.7e, the surface tension predictions of the ML algorithm are compared to the surface tension values that were

used as input in Equation (2.25). The diagonal line represents the ideal case where all ML predictions are in agreement with the surface tension values of Equation (2.25). Hence, it is evident that the ML algorithm is capable of predicting with high accuracy the surface tension of in-silico data. In Figure 4.7f, the error distribution of the predictions is shown. It is observed that the majority of the error is in the range of $\pm$ 0.25 mN/m, which is below the statistical error of traditional surface tension measurement techniques. The mean absolute error of the predictions was found to be 0.08 mN/m.

Subsequently, the ability of the ML algorithm to determine the surface tension on in-silico data with noise was investigated. In Figure 4.8a, is shown overlapping contours with increased added noise on the coordinates. The average mean absolute errors of the corresponding ML predictions are plotted in Figure 4.8b. It is seen that the MAE increases linearly as the noise increases. Figure 4.8c shows the error distribution of the predictions with added contour noise. The error distribution becomes broader as the contour noise increases, as expected. In the extreme case of 5 pxl added noise, the majority of the prediction error is between ± 2 mN/m, while the average MAE is below 1.2 mN/m. A simple function that defines an extreme case where all predictions are equal to the average value of surface tension from the training dataset was used as a prediction error baseline for the case where the neural network predicts randomly [31]. The mean absolute error calculated from that function was 10.1 mN/m. Since the maximum recorded MAE on in-silico data with noise was below 10.1 mN/m, it is indicated that the neural network does not predict in a random manner, even though the error has increased.

In Figure 4.8d, the maximum tilting angles applied on the contours towards the left and right directions are shown. In Figure 4.8e, the relation between the average MAE of the predictions and the maximum tilting angle is shown. Overall, the MAE increased when tilting takes place, however, there is no clear correlation between the tilting angle and the MAE. In Figure 4.8f, the error distribution of the predictions when tilting is added is shown. The prediction error was lower in comparison to the error induced when contour noise is added, with a range of prediction error ± 1 mN/m, while the maximum MAE recorded was approximately 0.25 mN/m. It can be hypothesized that the reason why tilting is not affecting the predictions significantly is that the majority of the contours tend to be circular. As a result, the tilting does not change the value of the radius significantly. However, the

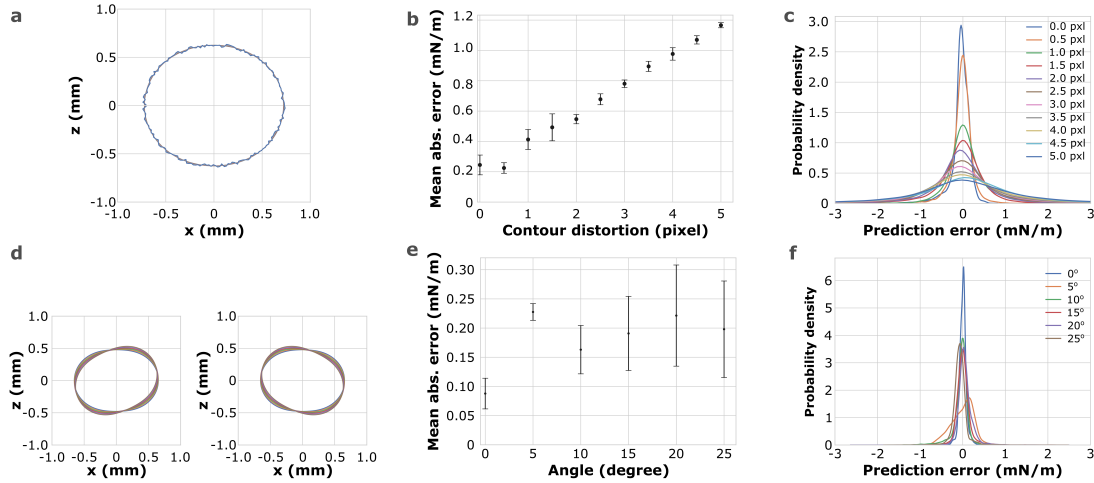experimental data were corrected for potential tilting to prevent this potential issue.

Figure 4.8: (a) Overlapping contours with increased added noise on the contour coordinates. (b) Relation between the added contour noise and the mean absolute error (MAE) of the ML predictions. (c) Error distribution of the ML predictions with respect to the added contour noise, (d) Overlapping contours with increased tilting. (e) Relation between the added tilting and the mean absolute error (MAE) of the ML predictions. (f) Error distribution of the ML predictions with respect to the added tilting.

4.2.2 Experimental data

In Figure 4.9a-c, the distributions of the surface tension, volume, and voltage of the chosen experimental data are shown. In Figure 4.9d, representative overlapping contours of levitated droplets are displayed. It is noted that the experimental contours are larger in size and deviate more from a circular shape, in comparison to the theoretical ones (Figure 4.7d).

The accuracy of the ML predictions on experimental contours was evaluated in Figures 4.9e-f and 4.10. Initially, the surface tension predictions made by the ML algorithm were compared to the surface tension values measured through the pendant drop method (Figure 4.9e). The majority of the ML predictions were in agreement with the pendant drop method. In Figure 4.9f, the error distribution of

the ML predictions is shown, and the majority of the predictions were in the range of ± 2 mN/m, while the average MAE was 0.88 mN/m.
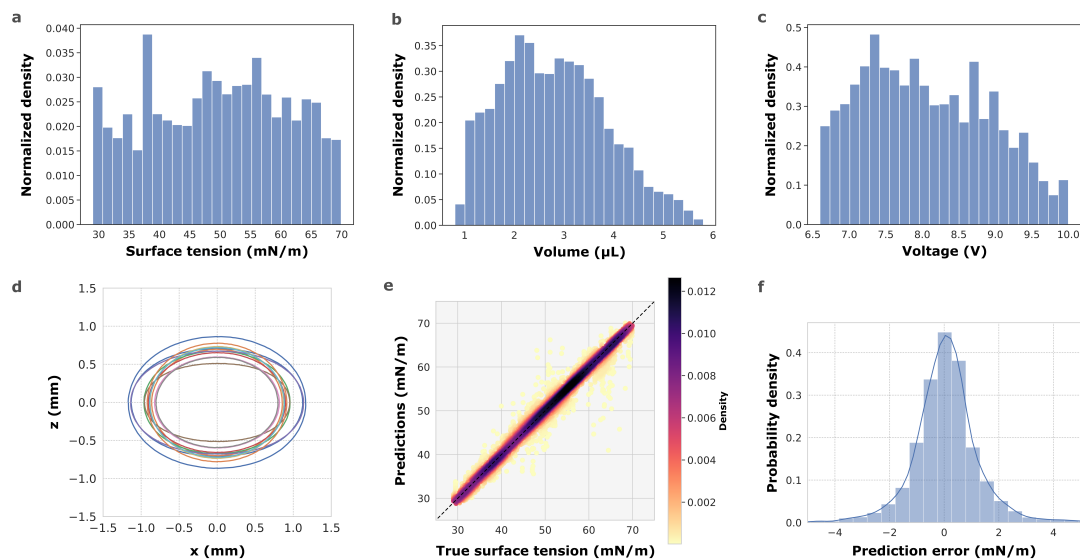

Figure 4.9: Data distributions of (a) surface tension, (b) volume, (c) voltage of experimental data. (d) Representative overlapping contours of experimental data. (e) Comparison between the surface tension values measured through the pendant drop method (x-axis) and the surface tension values predicted through the ML algorithm (y-axis) on the test dataset (11,674 instances). (f) Error distribution of the surface tension predictions the ML algorithm made on the test dataset (11,674 instances).

In Figure 4.10a-c, 100 randomly chosen ML predictions are plotted with respect to the adsorption isotherms of SDS, CTAB, and TritonX-100, respectively. Overall, the predictions cover the isotherm at a satisfactory level and the majority of the predictions appear to be in very good agreement with the pendant drop measurements.

The physical validity of the predictions made by the neural network was evaluated through a permutation algorithm, which shuffles the order of one feature and calculates how much the mean absolute error increased. A feature is considered more important, as the prediction error due to the shuffling increases, since it shows that the neural network depended more on that feature to reach a correct prediction. In Figure 4.11a, it is shown that the 175 radii have cumulatively the highest

influence on the prediction of surface tension, followed by the voltage, the current, and the vertical position. However, as shown in Figure 4.11b, each radius has a different influence degree on the predictions. It is seen that mainly the extreme contour points (darker in color) have the highest importance, which is expected since those points vary more notably when the droplet is deformed. Additionally, the remaining three input features are directly correlated to the acoustic pressure that is experienced on the surface of the droplet, with the driving voltage having the greatest influence on the predictions. On the whole, it is shown that the neural network weighs the input features in a manner that reflects reality adequately.
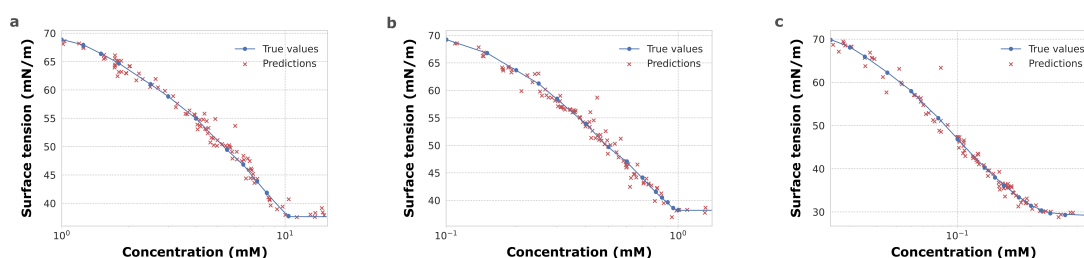

Figure 4.10: Comparison between the adsorption isotherm curves (*True values*) and 100 randomly distributed ML predictions of (a) sodium dodecylsulfate (SDS), (b) cetyltrimethylammonium bromide (CTAB), and (c) octylphenol decaethylene glycol ether (TritonX-100).

To identify potential error correlations between the predictions and the size or deformation of the droplets, the data distribution of these parameters is compared to the prediction MAE that was found for those values. The aspect ratio is used as a parameter to describe the deformation of the droplets. It is ranging between 0 and 1, 1 being for spherical droplets, while values below 1 indicate deformed droplets. By comparing Figure 4.11c with Figure 4.11d, no clear correlation between the volume distribution and the prediction MAE is observed. Similarly, for Figure 4.11e and Figure 4.11f, no correlation was observed between the prediction MAE and the aspect ratio of the droplets.
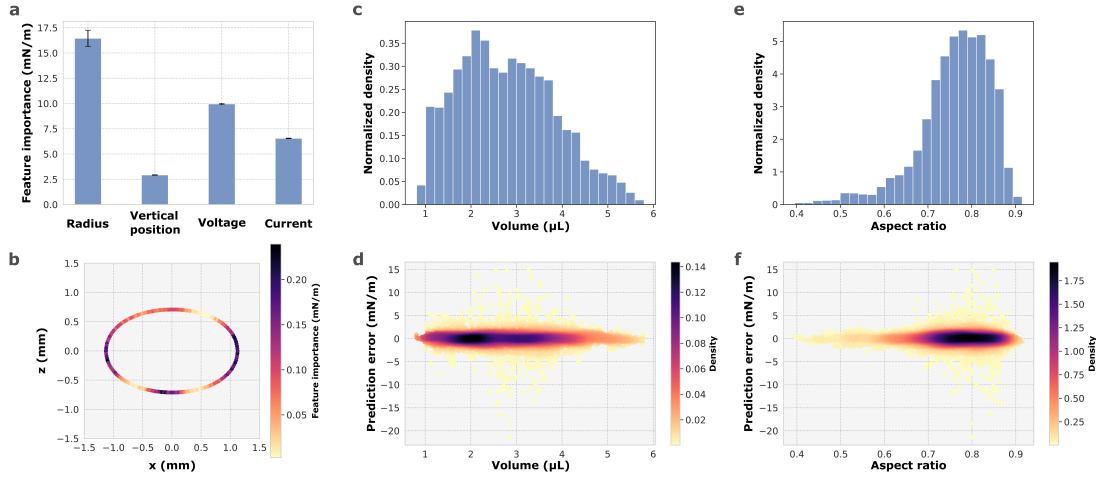
Figure 4.11: (a)The influence of each feature that was input in the neural network is expressed as feature importance. (b) The influence of each radius that defined the droplet contour on the machine learning predictions is color coded. The darker the color of the point, the higher the influence on the prediction. (c) Density distribution of volume in the test dataset. (d) Prediction error with respect to the volume of the droplet. (e) Density distribution of volume in the test dataset. (f) Prediction error with respect to the aspect ratio of the droplet.

5

Concluding remarks and future work

Acoustic levitation presents numerous possibilities for the study of small-volume samples in a contact-free manner. Recent studies on multiple-transducers acoustic levitators [9] [10] [14] [30], have enhanced the theoretical framework and levitation performance. However, for the implementation of acoustic levitation towards physicochemical studies, further development is required.

In this thesis, three customized designs of acoustic levitators (Mk1, Mk2, and Mk3) were theoretically and experimentally evaluated. The transducers of levitators Mk1 and Mk2 were positioned in a circular arrangement, while for Mk3 a hexagonal packing was implemented. Based on the simulations, levitator Mk3 presented the highest acoustic pressure in all dimensional planes (*i.e.*, xz, yz, and xy), while Mk1 and Mk2 exhibited similar levels of acoustic pressure, despite the difference in cavity length, and the number of transducers. Furthermore, the frequency response diagrams can be used as a guideline for finding the optimal operating frequency of a specific levitator.

In terms of experimental performance, levitator Mk3 presented the highest spatial stability, and levitation capacity, which was in line with the simulations. Levitators Mk1 and Mk2 presented similar spatial stability and levitation capacity. However, Mk1 showed higher horizontal stability in comparison to Mk2, potentially due to induced curl forces in the force field of levitator Mk2. Additionally, arranging the transducers in a hexagonal pattern was beneficial in the experimental performance

of the acoustic levitator. The outcome of this study was implemented into an interactive online framework, which allows the customization of acoustic levitators, for specific applications. Further development will now be leaning towards preventing uncontrolled rotation of the droplet that is sometimes observed by applying the approach by Cox *et al.* [9].

The adequate stability of levitator Mk1 allowed the acquisition of a large dataset of acoustically levitated aqueous surfactant droplets, under various conditions. However, the effect of the acoustic radiation force could not be directly related to the deformation and the surface tension through the existing models. Machine learning was therefore utilized as a tool to determine the underlying correlations between the droplet contours, and the surface tension, without any set preconditions. Droplets from a series of surfactant solutions (SDS, CTAB, and TritonX-100) were acoustically levitated over a period of 30 min, while the voltage was continuously altered, and in total over 50,000 photographs of droplets were collected. The neural network allowed the accurate determination of surface tension throughout the adsorption isotherms of all three surfactants (MAE = 0.88 mN/m). Moreover, the machine learning algorithm surpassed physical conditions and restrictions that were assigned in previous theoretical models, while the accuracy remained equally high, and in certain cases higher.

Through the experimental developments achieved in this work, we have accomplished to acoustically levitate liquid samples and acquire Nuclear Magnetic Resonance data, with a demagnetized version of levitator Mk3. Future work will focus on the study of more complex soft matter systems, such as pH-responsive gels and hybrid colloids inside and outside a magnetic field.

Acknowledgments

References

[1] Richard JK Weber et al. "Acoustic levitation: recent developments and emerging opportunities in biomaterials research". In: *European Biophysics Journal* 41.4 (2012). DOI: 10.1007/s00249-011-0767-3, pp. 397–403.

[2] Wei-Hsuan Sung et al. "Small-volume detection: platform developments for clinically-relevant applications". In: *Journal of Nanobiotechnology* 19.1 (2021). DOI: 10.1186/s12951-021-00852-1, pp. 1–14.

[3] Constantin Chilowsky and Paul Langevin. *Production of submarine signals and the location of submarine objects*. US Patent, US1471547A. Oct. 1923.

[4] Guy Reginald Dunlop. "Ultrasonic transmission imaging". DOI: 10.26021/10874. PhD dissertation. University of Canterbury, 1978.

[5] Yuren Tian, R Glynn Holt, and Robert E Apfel. "Deformation and location of an acoustically levitated liquid drop". In: *The Journal of the Acoustical Society of America* 93.6 (1993). DOI: 10.1121/1.415384, pp. 3096–3104.

[6] Marco AB Andrade et al. "Experimental investigation of the particle oscillation instability in a single-axis acoustic levitator". In: *AIP Advances* 9.3 (2019). DOI: 10.1063/1.5078948, p. 035020.

[7] JKR Weber et al. "Acoustic levitator for structure measurements on low temperature liquid droplets". In: *Review of Scientific Instruments* 80.8 (2009), p. 083904.

[8] Asier Marzo, Tom Corkett, and Bruce W Drinkwater. "Ultraino: An open phased-array system for narrowband airborne ultrasound transmission". In: *IEEE Transactions on Ultrasonics, Ferroelectrics, and Frequency Control* 65.1 (2017), pp. 102–111.

[9] Luke Cox et al. "Acoustic lock: Position and orientation trapping of non-spherical sub-wavelength particles in mid-air using a single-axis acoustic levitator". In: *Applied Physics Letters* 113.5 (2018), p. 054101.

[10]   Themis Omirou et al. "LeviPath: Modular acoustic levitation for 3D path visualisations". In: *Proceedings of the 33rd Annual ACM Conference on Human Factors in Computing Systems*. 2015, pp. 309–312.

[11]   Asier Marzo et al. "Holographic acoustic elements for manipulation of levitated objects". In: *Nature Communications* 6.1 (2015), pp. 1–7.

[12]   Asier Marzo and Bruce W Drinkwater. "Holographic acoustic tweezers". In: *Proceedings of the National Academy of Sciences* 116.1 (2019), pp. 84–89.

[13]   Ayumu Watanabe, Koji Hasegawa, and Yutaka Abe. "Contactless fluid manipulation in air: Droplet coalescence and active mixing by acoustic levitation". In: *Scientific Reports* 8.1 (2018). DOI: 10.1038/s41598-018-28451-5, pp. 1–8.

[14]   Asier Marzo, Adrian Barnes, and Bruce W Drinkwater. "TinyLev: A multi-emitter single-axis acoustic levitator". In: *Review of Scientific Instruments* 88.8 (2017). DOI: 10.1063/1.4989995, p. 085105.

[15]   Vicente Romero-Garcia and Anne-Christine Hladky-Hennion. *Fundamentals and applications of acoustic metamaterials: from seismic to radio frequency*. John Wiley & Sons, 2019.

[16]   Bengt O Enflo and Claes M Hedberg. "Physical theory of nonlinear acoustics". In: *Theory of Nonlinear Acoustics in Fluids* (2002), pp. 11–29.

[17]   *Levitate*. https://github.com/AppliedAcousticsChalmers/levitate. 2021.

[18]   Antonio Arnau. *Piezoelectric transducers and applications*. Vol. 2004. Springer, 2004.

[19]   Thomas Young. "III. An essay on the cohesion of fluids". In: *Philosophical Transactions of the Royal Society of London* 95 (1805), pp. 65–87.

[20]   Pierre Simon marquis de Laplace. *Supplément à la Théorie de l'action capillaire*. Courcier, 1807.

[21]   Eugene H Trinh and Chaur-Jian Hsu. "Equilibrium shapes of acoustically levitated drops". In: *The Journal of the Acoustical Society of America* 79.5 (1986). DOI: 10.1121/1.393660, pp. 1335–1338.

[22]   Lev Petrovich Gor'kov. "On the forces acting on a small particle in an acoustical field in an ideal fluid". In: *Soviet Physics—Doklady*. Vol. 6. 1962, pp. 773–775.

[23]   Philip L Marston. "Shape oscillation and static deformation of drops and bubbles driven by modulated radiation stresses—Theory". In: *The Journal of*

the Acoustical Society of America 67.1 (1980). DOI: 10.1121/1.383798, pp. 15–26.

[24] Philip L Marston, Salvo E LoPorto–Arione, and Glenn L Pullen. "Quadrupole projection of the radiation pressure on a compressible sphere". In: *The Journal of the Acoustical Society of America* 69.5 (1981). DOI: 10.1121/1.385785, pp. 1499–1501.

[25] Alexander N Kalashnikov and Richard E Challis. "Errors and uncertainties in the measurement of ultrasonic wave attenuation and phase velocity". In: *IEEE Transactions on Ultrasonics, Ferroelectrics, and Frequency Control* 52.10 (2005), pp. 1754–1768.

[26] Yuren Tian, R Glynn Holt, and Robert E Apfel. "A new method for measuring liquid surface tension with acoustic levitation". In: *Review of Scientific Instruments* 66.5 (1995). DOI: 10.1063/1.1145506, pp. 3349–3354.

[27] Jon Paul Janet and HeatherJ Kulik. *Machine Learning in Chemistry*. American Chemical Society, 2020.

[28] Aaron Fisher, Cynthia Rudin, and Francesca Dominici. "All Models are Wrong, but Many are Useful: Learning a Variable's Importance by Studying an Entire Class of Prediction Models Simultaneously." In: *Journal of Machine Learning Research* 20.177 (2019), pp. 1–81.

[29] Marco AB Andrade, Flavio Buiochi, and Julio C Adamowski. "Finite element analysis and optimization of a single-axis acoustic levitator". In: *IEEE Transactions on Ultrasonics, Ferroelectrics, and Frequency Control* 57.2 (2010), pp. 469–479.

[30] Carl Andersson and Jens Ahrens. "Reducing spiraling in transducer array based acoustic levitation". In: *2020 IEEE International Ultrasonics Symposium (IUS)*. IEEE. 2020, pp. 1–4.

[31] F. Pedregosa et al. "Scikit-learn: Machine Learning in Python". In: *Journal of Machine Learning Research* 12 (2011), pp. 2825–2830.